Surface Science 606 (2012) 846–851

Contents lists available at SciVerse ScienceDirect

Surface Science

journal homepage: www.elsevier.com/locate/susc

An STM study of the initial oxidation of single-crystalline zirconium surfaces

Georgijs Bakradze [a], Lars P.H. Jeurgens [a,*], Eric J. Mittemeijer [a,b]

[a] Max Planck Institute for Intelligent Systems (formerly Max Planck Institute for Metals Research), Heisenbergstraße 3, D-70569 Stuttgart, Germany
[b] Institute for Materials Science, University of Stuttgart, Germany

ARTICLE INFO

Article history:
Received 20 September 2011
Accepted 31 January 2012
Available online 9 February 2012

Keywords:
Oxidation
Zirconium oxide
Scanning tunneling microscopy
Crystallization
Surface structure, morphology, roughness and topography
Thin oxide films

ABSTRACT

The microstructural development of thin (thickness < 10 nm) oxide layers grown on Zr surfaces by thermal oxidation was investigated by in-vacuo STM and XPS. To this end, single-crystalline Zr(0001) and Zr($10\bar{1}0$) surfaces were prepared under UHV conditions by a cyclic treatment of ion-sputtering and in-vacuo annealing steps and then exposed to dry O_2(g) in the temperature range of 300–450 K (at $pO_2 = 1\times10^{-4}$ Pa). Oxidation proceeds by the fast formation of a dense arrangement of tiny oxide nuclei, which cover the entire Zr surface. The initial oxide cluster size is about 1.2 ± 0.1 nm. The transport processes on the oxidizing surface become promoted with increasing temperature and thereby the oxide clusters rearrange into bigger agglomerates with increasing oxidation time. At the same time, a long-range atomic order develops in the oxide overgrowths, as evidenced from the emergence of a bonding/non-bonding fine structure in the resolved oxide-film upper valence band, as measured in-situ by XPS.

1. Introduction

The dry oxidation of metals by molecular oxygen is still among the most extensively (both experimentally and theoretically) studied heterogeneous gas–solid reactions [1–4]. Thin oxide films, as formed on metallic (or semi-conductor) substrate surfaces in an oxidizing environment, influence important properties of such components, such as the corrosion resistance, the thermal stability, the catalytic activity and the electrical, adhesive and tribological properties.

The majority of initial stage oxidation studies of metallic surfaces have hitherto focused on: (i) the determination of oxidation-rate laws (i.e. the oxidation kinetics) as a function of the oxidation conditions [2,5], and on (ii) the characterization of the developing oxide (micro) structure and the chemical constitution [6–9]. The information on the amorphous/crystal structure of very thin (<10 nm) oxide films, as formed on metal and alloy surfaces under oxidizing conditions at low temperatures (up to, say, 500 K), is usually derived from observations in reciprocal space using diffraction techniques: e.g. low energy electron diffraction (LEED) [10,11], surface X-ray diffraction [12], transmission electron diffraction [13,14]. On the other hand, the chemical constitution of such thin oxide films is typically determined by spectroscopic techniques, such as X-ray Photoelectron Spectroscopy (XPS) or Auger-electron spectroscopy (see e.g. [11–13]). Although the *microstructural* characteristics of the developing oxide film play a crucial role for many important material properties (see above), the above mentioned diffraction and spectroscopic techniques do not provide *direct* information on the developing oxide morphology.

Direct microscopic imaging, in real space and down to the atomic scale, of the surface morphology of very thin oxide films can typically only be performed by transmission electron microscopy (TEM) [9,15] or scanning tunnelling microscopy (STM). Hence, since the advent of STM in 1981, numerous STM studies on the initial stage of thermal oxidation of metallic surfaces have been published, e.g. for Al(111) [16], Cr(110) [17,18], Cu(111) [19–21], Fe(110) [22], Fe(111) [23], Mg(0001) [24], Ni_3Al(110) [25], Pt(110) [26], Rh(111) [27] and W(110) [28]. These studies have shown that the initial stages of oxidation of metallic surfaces typically proceed by a series of consecutive, but overlapping steps, such as (i) oxygen chemisorption, (ii) oxide nucleation and (iii) continued growth of the oxide nuclei until the entire metal surface has been covered with oxide (i.e. a "closed" oxide film has been formed). At low oxidation temperatures, after an initial, very fast oxide-film growth regime, the transport rate of the migrating species through the closed oxide film becomes negligible upon continued exposure to oxygen, which results in a so-called passivating behaviour (see Ref. [29] and Section 2.1). At higher oxidation temperatures, on the other hand, the initial, fast oxide-film growth regime is generally succeeded by a stage of slower oxidation corresponding with a continuous thickening of the insulating oxide film [29–31]. STM investigations at such later stages of the oxidation process are often complicated by experimental problems, such as unstable tunneling contacts (in particular for thick insulating oxide films) [32].

To our knowledge, no STM studies on the thermal surface oxidation of Zr or its alloys have been presented so far. Few STM studies have been reported on the growth of ZrO_2 on *foreign* metal surfaces, such as Ag(100) [33] and Pt(111) [34], by reactive deposition of Zr in an oxygen

* Corresponding author.Present adress: Empa, Swiss Federal Laboratories for Materials Science and Technology, Überlandstrasse 129, 8600 Dübendorf, Switzerland. Tel.: +41 58 765 4053; fax: +41 58 765 4011.
E-mail address: lars.jeurgens@empa.ch (L.P.H. Jeurgens).

0039-6028/$ – see front matter © 2012 Elsevier B.V. All rights reserved.
doi:10.1016/j.susc.2012.01.026

atmosphere (with and without subsequent annealing), which clearly is a very different growth process. Comprehensive knowledge on the oxidation behaviour of zirconium metal surfaces is required in many technological areas, such as corrosion protection [35], heterogeneous catalysis/electrochemistry [36,37] and microelectronics [38,39]. Against this background the present *in-vacuo* STM study addresses the initial stages of the dry, thermal oxidation of bare single-crystalline Zr(0001) and Zr(10$\bar{1}$0) surfaces in the temperature range of 300–450 K and at a partial oxygen gas pressure of $pO_2 = 1\times10^{-4}$ Pa. As demonstrated in this work, the STM observations on the evolving surface topography of the oxide overgrowths on the Zr(0001) and Zr(10$\bar{1}$0) surfaces are complementary to earlier reported results on: (i) the oxide-film growth kinetics, as obtained by real-time in-situ spectroscopic ellipsometry (RISE) [29,45], and (ii) the evolution of the oxide-film microstructure, as derived from oxide-film valence-band (VB) studies by XPS [40–42,48].

2. Experimental procedures

Disc-shaped Zr(0001) and Zr(10 $\bar{1}$0) single crystals were cut (diameter 6 mm; 1 mm thick; orientation alignment within ±0.5° of the nominal surface plane) from a single-crystalline unalloyed α-Zr rod and subsequently single-side mechanically polished (last step 0.05 μm). Main impurities in the polished specimens, as identified by inductively coupled plasma optical emission spectroscopy analysis, are (in mass parts): Hf (60 ppm); Fe (25 ppm); Ti (1 ppm); Cu, Zn, Mn, Ca, Na (<2 ppm).

The polished specimens were introduced into a combined ultrahigh vacuum (UHV) system, possessing facilities for sputter-cleaning (SC) and XPS and STM analyses (base pressure $<5\times10^{-8}$ Pa). Next, the (native) oxide and other adventitious contaminants (mainly C) on the surface were removed by SC, first with 3 keV Ar^+ ions and subsequently with 1 keV Ar^+ ions (see what follows), rastering the entire surface area, until no other element than Zr was detected in a measured XPS survey spectrum (see below). Roughening of the ion-bombarded single-crystalline surfaces due to local differences in the sputter yield by ion channelling and shadowing effects [44] was suppressed by employing continuous specimen rotation at a speed of about 2 rpm during the SC treatments. The SC was performed with 3 keV Ar^+ ions until all C surface contamination was removed (as verified by XPS); all subsequent SC treatments (e.g. to remove remaining O contamination) were performed with 1 keV Ar^+ ions. Next, the specimen and specimen holder were outgassed by a cycling treatment of alternating 1 kV Ar^+ SC and in-vacuo annealing steps, while gradually increasing the specimen temperature during each successive in-vacuo annealing step up to 1000 K. As a final surface preparation step prior to each oxidation experiment, the sputter-cleaned surfaces were in-vacuo annealed at 1000 K for 300–600 s.

The SC treatment destroys the crystallinity at the specimen surface and also induces sputter-induced surface roughness (see Section 2.1). However, the surface crystallinity in the ion-bombarded surface region is fully restored (as verified by in-situ LEED in Ref. [45]) and the surface becomes atomically flat (as evidenced by in-situ STM in this work; see Section 2.1) during the final in-vacuo annealing step at 1000 K for 300–600 s. The single-crystalline Zr(0001) and Zr(10$\bar{1}$0) surfaces, as obtained after the final in-vacuo annealing step, are further designated as *bare* Zr surfaces.

Next, oxide films were grown at 300, 375 and 450 K by exposure of the bare Zr(0001) and Zr(10$\bar{1}$0) surfaces for different times to pure oxygen gas (purity ≥ 99.9999 vol.% with a specified residual gas content of $H_2O \le 0.5$ vpm, $N_2 + Ar \le 2.0$ vpm, $C_nH_m \le 0.1$ vpm and $CO_2 \le 0.1$ vpm) at $pO_2 = 1\times10^{-4}$ Pa. The oxidation temperature was measured with a type K thermocouple, which was put in direct mechanical contact with the single-crystal surface.

XPS was applied to determine the chemical constitution of the sputter-cleaned, annealed and oxidized surfaces. The XPS analysis was performed with a Thermo VG Thetaprobe system employing monochromatic Al Kα radiation ($h\nu = 1486.68$ eV). XPS survey spectra, covering a binding energy (BE) range from 0 to 1200 eV, were recorded with a step size and pass energy of 0.2 eV and of 200 eV, respectively.

The STM studies of the bare and oxidized Zr surfaces (after cooling down to room temperature) were performed in an UHV side-chamber (base pressure $<8\times10^{-9}$ Pa), which is interconnected to the UHV chambers for in-situ oxidation and in-situ AR-XPS analysis. The STM investigations were performed with a Specs Aarhus 150 Scanning Tunnelling Microscope (Createc edition), operated in constant tunnelling current (topographic) mode, as controlled by the Specs SPC-260 electronics. "Imaging" (i.e. mapping) was performed at room temperature by scanning the surface employing a steady state positive specimen bias voltage (V_t) in the range of 0.3–2.7 V and a constant tunnelling current (I_t) in the range of 0.2–1.5 nA (see figure captions for the values of I_t, V_t and the maximum height difference, ΔZ; in the topographic images shown the fast-scanning direction is horizontal). Before the STM investigation, the electrochemically etched tungsten tip was cleaned in-situ by sputtering for 900 s with a parallel (defocussed) 3 keV Ar^+ beam (total sputter current of about 1.5 μA). Also during the subsequent STM investigation (i.e. while scanning the specimen surface), the tip was repeatedly cleaned and sharpened by shortly pulsing (for about 0.1 s) of the specimen bias voltage up to about 10 V (on specimen areas different from those investigated). The obtained STM images were post-processed (with the help of common filters like background subtraction, flatten etc.) with the WSxM 4.0 software [46]. The average lateral size of the oxide clusters was obtained from individual line scans of the recorded STM images by determining the full-width-at-half-the-maximum-height values of a total of 20–30 oxide clusters per image.

2.1. Evolution of the oxide-film microstructure with temperature in the range 300–450 K

Exemplary STM images, as recorded from the bare (i.e. sputter-cleaned and annealed) Zr substrates after different stages of the in-vacuo specimen preparation procedure (see Section 2) are shown in Fig. 1a–c. Evidently, the rough Zr surface, as obtained after the initial SC treatment (see Fig. 1a), becomes atomically flat and single-crystalline by the final in-vacuo annealing step at 1000 K for 300–600 s: see Fig. 1b and see corresponding LEED patterns of the bare Zr surfaces, as presented in Ref. [45]. The measured individual step heights of about 2.5 Å between the atomically flat terraces on the bare Zr(10$\bar{1}$0) surface (see Fig. 1b) closely match the (ideal) interplane distance of 2.8 Å along the α-Zr[10$\bar{1}$0] direction and thus represent mono-atomic steps. The striped appearance of the bare Zr(10 $\bar{1}$0) terraces (see Fig. 1b) is due to a 1×4 reconstruction of the (10$\bar{1}$0) crystal surface of α-Zr, as reported in Ref. [11].

The bare Zr surfaces are highly reactive and therefore easily contaminate (typically within 1800 s) with rest-gas species in the UHV chamber (e.g. CO and H_2O), even at a base pressure as low as 1×10^{-8} Pa (as shown by STM and XPS). An STM image of an adsorbate-contaminated bare Zr(0001) surface (in-situ XPS analysis indicated that O is the main surface contaminant) is shown in Fig. 1c.

As demonstrated by RISE [29,45], exposure of the bare single-crystalline Zr surfaces to pure O_2(g) at $pO_2 = 1\times10^{-4}$ Pa at a constant substrate temperature in the range of 300–450 K results in the very fast (i.e. within 500 to 1900 s) formation of a closed oxide film, which attains a near-limiting thickness at $T<375$ K. The total oxide-film thickness, as attained after 7200 s of oxidation (relevant to the STM images shown in Figs. 2 and 3 discussed below) increases with increasing oxidation temperature from about 1.3 nm at $T=300$ K to 9.2 nm at $T=450$ K: see Table 1. For $T>375$ K, the more open Zr(10$\bar{1}$0) prism plane oxidizes more readily than the densely packed Zr(0001) basal plane, in particular at the higher temperatures [29,45].

Representative STM images of the Zr(0001) and Zr(10$\bar{1}$0) surfaces after 7200 s of oxidation at 300 K and 375 K (i.e. after reaching near-

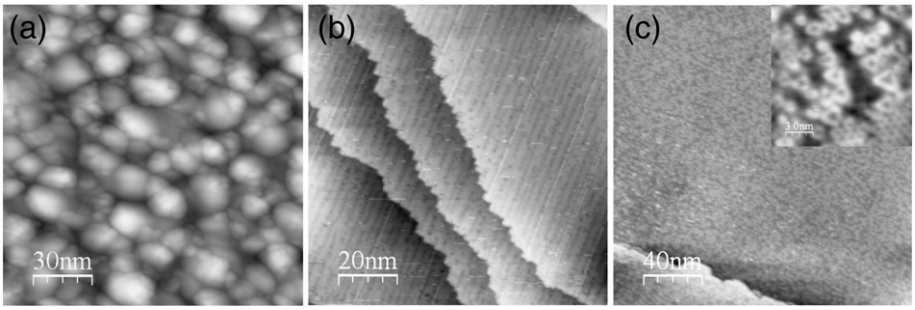

Fig. 1. STM images (see Section 2) as recorded in-situ from: (a) the Zr(10$\bar{1}$0) surface after sputter-cleaning (SC) with 3 keV Ar^+ for 3 h; (b) the sputter-cleaned Zr(10$\bar{1}$0) surface after annealing at 1000 K for 900 s; (c) the Zr(0001) surface (i.e. sputter-cleaned and annealed as in (b)) after residing for 1800 s under UHV conditions. The adsorbed contaminant atoms (predominantly oxygen) form triangled structures (see inset). (a) $V_t = 1.8$ V, $I_t = 0.240$ nA, $\Delta Z = 19.2$ nm; (b) $V_t = 0.4$ V, $I_t = 0.330$ nA, $\Delta Z = 0.5$ nm; (c) $V_t = 2.1$ V, $I_t = 0.250$ nA, $\Delta Z = 0.7$ nm; insert in (c) $V_t = 0.7$ V, $I_t = 1.320$ nA, $\Delta Z = 0.2$ nm.

limiting oxide-film thicknesses) are shown in Fig. 2a to d. STM images of the Zr(0001) and Zr(10$\bar{1}$0) surfaces after 7200 s of oxidation at 450 K (corresponding to the highest oxidation temperature applied in the present study) are shown in Fig. 3e and j, respectively.

Evidently, the STM images of the bare and oxidized surfaces (cf. Figs. 1b and 2c for the Zr(10$\bar{1}$0) surface) are strikingly different. The atomically-flat terraces, characteristic for the bare Zr surfaces (Fig. 1b), are covered with irregular protrusions after oxidation. The protrusions on both oxidized surfaces are constituted of very small oxide *clusters*, as indicated in Fig. 2a. The values for the average lateral sizes of the oxide clusters at $t = 7200$ s for various oxidation temperatures in the range of $T = 300$–450 K have been gathered in Table 1. Similar irregular oxide morphologies have been observed by STM for oxidized Cr(110) surfaces (after 0.75 L O_2-exposure at 300 K [18]), oxidized Cu(111) surfaces (after 970 L O_2-exposure at 300 K [19]), oxidized Fe(111) surfaces (after 400 L O_2-exposure at 300 K [23]) and oxidized $Cu_{0.7}Zn_{0.3}$(111) surfaces (after O_2-exposures up to 1280 L at 300 K [47]). Such small oxide clusters have been previously designated as "grains of the oxide film" [18], "oxide islands" [23,47] or "adsorbed oxygen (clusters)" [47]. Although the average size of these initial oxide clusters (i.e. with an average diameter of about 1 nm, see Table 1 and Section 2.2) by far exceeds the lattice parameter of zirconium or zirconia, the atomic structure of the clusters could not be resolved by STM (as performed at RT), as also holds for the STM analysis of similar oxide structures, as formed during RT oxidation of Cr(110), Fe(110) and Ni surfaces [17,27].

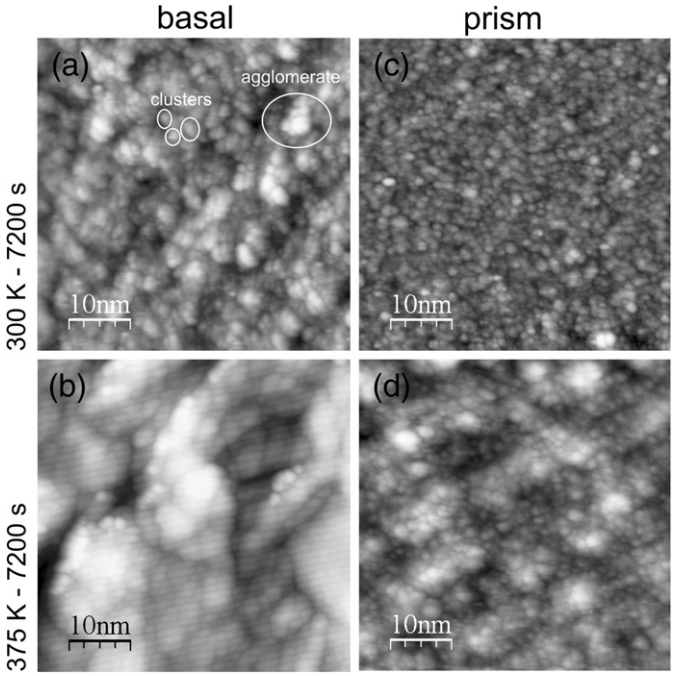

Fig. 2. STM images (see Section 2) as recorded in-situ from the Zr(0001) (left panels a and b) and Zr(10$\bar{1}$0) (right panels c and d) surfaces after oxidation for 7200 s at $pO_2 = 1\times10^{-4}$ Pa at T = 300 K (upper panels a and c) and 375 K (lower panels b and d). (a) $V_t = 2.8$ V, $I_t = 0.640$ nA, $\Delta Z = 1.0$ nm; (b) $V_t = 0.6$ V, $I_t = 0.400$ nA, $\Delta Z = 1.5$ nm; (c) $V_t = 2.2$ V, $I_t = 0.210$ nA, $\Delta Z = 0.8$ nm; (d) $V_t = 2.9$ V, $I_t = 0.790$ nA, $\Delta Z = 1.8$ nm. The nearly horizontal stripes in image (b) present a nonrecurring experimental artefact.

The designation "oxide grains" (cf. Ref. [18]) implicitly assumes a crystalline structure of the oxide overgrowth. However, the oxide layers, as grown on Zr(0001) and Zr(10$\bar{1}$0) surfaces at $T<400$ K (see Fig. 2), are amorphous as demonstrated by LEED, RHEED and XPS VB studies (see Section 2.2 and Ref. [48]). The term "oxide islands" (cf. Refs. [23,47]), on the other hand suggests the existence of bare patches of metal surface in-between the "oxide islands" which were not observed in the recorded images. This indicates that the Zr(0001) and Zr(10$\bar{1}$0) surfaces at this stage of oxidation have been fully covered by oxide, in accordance with the drop of the oxidation rate associated with the occurrence of a near-limiting oxide-film thickness at $T<375$ K [29].

The in-situ XPS analysis,[1] performed on the surfaces of the oxidized specimens, only evidences the presence of *oxidic* states of Zr and O, indicating that the observed small protrusions do *not* pertain to chemisorbed O species (as referred to in Ref. [47]). Therefore, the small protrusions are denoted as "oxide clusters" (or "oxide nuclei", see Section 2.2).

The density of the oxide clusters is, on average, slightly lower on the oxidized Zr(0001) surface than on the oxidized Zr(10$\bar{1}$0) surface for the same oxidation conditions at $T = 300$ K, 375 K and 450 K (see Figs. 2a,c and 3). For all oxidation temperatures the average oxide cluster size (as indicated by the average cluster diameter d) after $t = 7200$ s is very similar for both surfaces; the average oxide cluster diameter for $t = 7200$ s increases from about $d = 1.4 \pm 0.2$ nm at $T = 300$ K to $d = 2.0 \pm 0.3$ nm at $T = 375$ K and to $d = 4.0 \pm 1.0$ nm at $T = 450$ K (almost independent of the substrate orientation): see Table 1 and Fig. 2.

An average oxide cluster size in the range of 1.2–4.2 nm, as determined for the oxidized Zr surfaces at $t = 7200$ s (corresponding to an O_2-exposure of 5400 L) for $T = 300$–450 K, is comparable to reported oxide cluster sizes of 4.0 ± 0.5 nm, for a Cr(110) surface after 80 L O_2-exposure at 300 K [18], and of 3.0–4.0 nm [22], for a Fe(110) surface after 80 L O_2-exposure at 300 K.

The thermally activated transport processes on the oxidizing surface become promoted with increasing temperature and, consequently, upon continued oxidation the oxide clusters coalesce into larger

[1] The in-situ STM and XPS analyses of the oxidized Zr surfaces were performed under UHV conditions (i.e. after evacuating the O_2 gas; see Section 2).

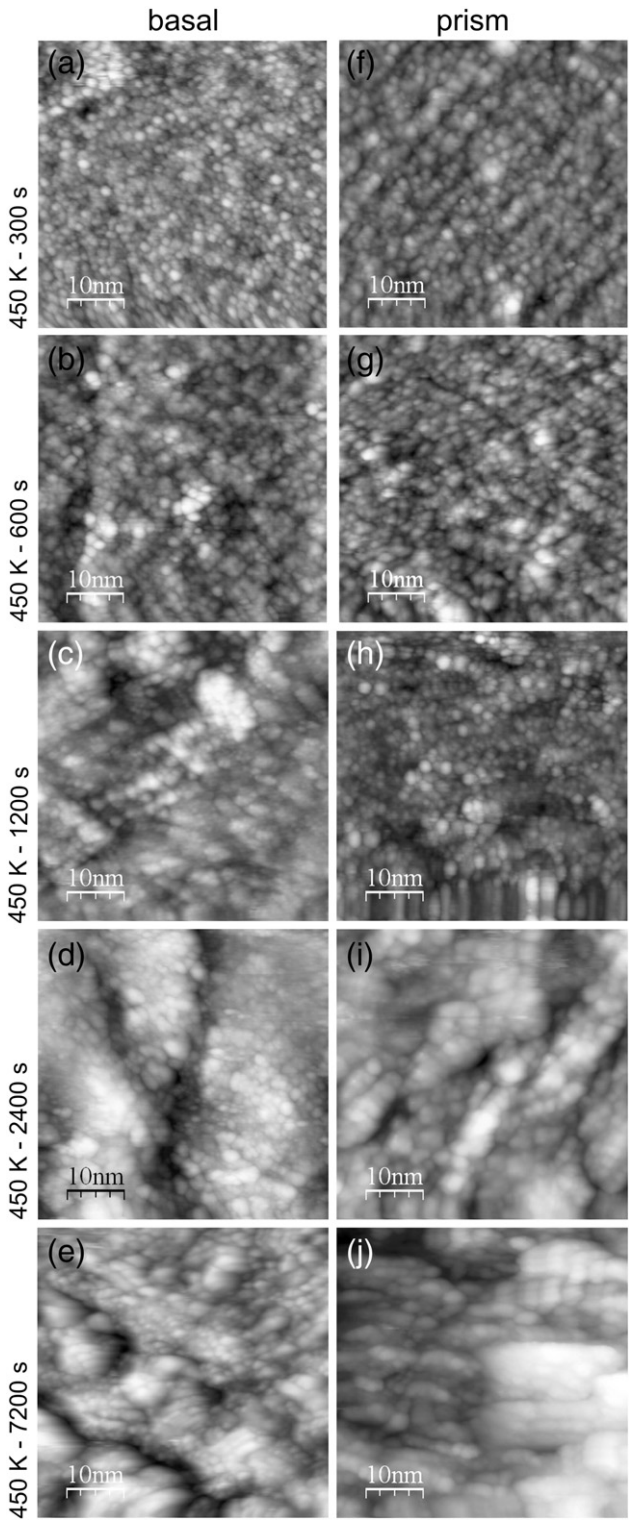

Fig. 3. STM images (see Section 2) as recorded in-situ from the (a–e) Zr(0001) and (f–j) Zr(10$\bar{1}$0) surfaces after oxidation at 450 K for 300 s, 600 s, 1200 s, 2400 s and 7200 s ($pO_2 = 1\times10^{-4}$ Pa). (a) $V_t = 2.2$ V, $I_t = 0.330$ nA, $\Delta Z = 1.4$ nm; (b) $V_t = 1.8$ V, $I_t = 0.110$ nA, $\Delta Z = 1.5$ nm; (c) $V_t = 1.3$ V, $I_t = 0.180$ nA, $\Delta Z = 2.8$ nm; (d) $V_t = 2.2$ V, $I_t = 0.610$ nA, $\Delta Z = 2.2$ nm; (e) $V_t = 2.8$ V, $I_t = 0.190$ nA, $\Delta Z = 4.1$ nm; (f) $V_t = 2.5$ V, $I_t = 0.750$ nA, $\Delta Z = 1.2$ nm; (g) $V_t = 2.7$ V, $I_t = 0.270$ nA, $\Delta Z = 1.0$ nm; (h) $V_t = 2.6$ V, $I_t = 0.200$ nA, $\Delta Z = 1.4$ nm; (i) $V_t = 2.6$ V, $I_t = 0.730$ nA, $\Delta Z = 4.4$ nm; (j) $V_t = 2.2$ V, $I_t = 0.990$ nA, $\Delta Z = 3.3$ nm.

agglomerates, which is apparent from the STM images for higher oxidation temperatures at $t = 7200$ s (see Figs. 2a, b, d and 3). Smaller oxide particles, encompassed by a surface of generally smaller radius of curvature, have, according to the Gibbs–Thomson relationship, a higher Gibbs energy than larger ones; thereby, a driving force for oxide-cluster coarsening, development of "agglomerates" by restructuring/reorientation, exists. The agglomerates do not show any specific regularities in shape and have different sizes; their average size is typically larger for the oxidized Zr(0001) surface than for the oxidized Zr(10$\bar{1}$0) surface (cf. Fig. 2b, d and Table 1).

Table 1
The average lateral size, d, of the oxide clusters (and its standard deviation σ_d), as determined from the recorded STM images of the oxidized Zr(0001) (basal) and Zr(10$\bar{1}$0) (prism) surfaces (oxidized for different times, t, at various temperatures, T, and at $pO_2 = 1\times10^{-4}$ Pa; see Figs. 2 and 3). The root-mean-squared roughness values, R_{rms}, (as determined from the corresponding STM images) are also given. The overall oxide-layer thickness values, L_{tot}, were obtained by real-time in-situ spectroscopic ellipsometry (RISE) [29,45].

T=		300 K	375 K	450 K				
t (s)		7200 s	7200 s	300 s	600 s	1200 s	2400 s	7200 s
Basal	d (nm)	1.4	1.8	1.2	1.9	2.0	3.0	3.9
	σ_d (nm)	0.2	0.2	0.1	0.1	0.2	0.3	1.5
	L_{tot} (nm)	1.3	2.6	1.5	1.9	2.5	3.5	6.5
	R_{rms} (nm)	0.2	0.3	0.2	0.2	0.6	0.5	0.6
Prism	d (nm)	1.4	1.7	1.6	2.3	2.2	3.3	4.2
	σ_d (nm)	0.1	0.2	0.2	0.2	0.2	0.4	1.3
	L_{tot} (nm)	1.4	2.9	2.5	3.0	4.3	6.0	9.2
	R_{rms} (nm)	0.1	0.3	0.1	0.2	0.2	0.9	0.6

As concluded on the basis of the abovementioned STM results in combination with the cross-sectional TEM analysis of the grown oxide films (as reported in Ref. [49]), the oxide agglomerates eventually constitute the oxide grains of the polycrystalline oxide layer that evolves upon prolonged oxidation at 450 K. The reduction of the total oxide-surface/interface area upon oxide-cluster agglomeration coarsens the oxide microstructure, which can cause a change of governing atomic transport mechanism (i.e. bulk vs. grain boundary transport) upon oxide growth, as indeed reported for the oxidation of Zr surfaces at 450 K in Ref. [49].

The fast occurrence of a limiting oxide-film thickness at $T<375$ K (see above discussion and Ref. [29]) evidently hinders a meaningful STM investigation of the successive stages of development of the oxide-layer microstructure with increasing time. At $T\geq450$ K, the retardation of the oxide-film growth rate, after the initial, fast oxidation regime, is much less pronounced and, instead, the oxide film grows continuously (i.e. a near-limiting oxide-film thickness is no longer established) [29]. A comparative STM study of the successive stages of development of the oxide-layer microstructure at $T = 450$ K is thus possible, which is presented in Section 2.2.

2.2. Evolution of the oxide-film microstructure with oxidation time at 450 K

The evolution of the oxide-layer microstructure, as monitored by STM, for successive oxidation times, $t = 300$, 600, 1200, 2400 and 7200 s, at $T = 450$ K is depicted for the Zr(0001) surface in Fig. 3a–e (i.e. left column of Fig. 3) and for the Zr(10$\bar{1}$0) surface in Fig. 3f–j (i.e. right column of Fig. 3). Note that these oxidation experiments have not been performed in a cumulative manner: i.e. for each oxidation time a freshly prepared, bare Zr substrate was utilized (see Section 2 for details). Consequently, the recorded STM images for one crystal plane after different oxidation times do not represent the same location of an oxidized surface.

After the first 300 s of oxidation at $T = 450$ K (equivalent to 0.75 L O_2-exposure at $pO_2 = 1\times10^{-4}$ Pa), the bare Zr(0001) and Zr(10$\bar{1}$0) surfaces are (already, cf. results for 7200 s at oxidation temperatures as low as 300 K, discussed in Section 2.1) densely covered with small oxide clusters (see Fig. 3a, f and Table 1). The lateral size of the oxide clusters gradually increases with increasing oxidation time: see Table 1 and Fig. 3. The initial lateral size of the oxide cluster is comparable with

the overall oxide-film thickness, L_{tot}, as determined by RISE [29,45] and reported in Table 1. At these low O_2-exposures (e.g. of 0.75 L; see Fig. 3a and f), the distribution of the lateral size of the oxide clusters is very narrow, which hints at either a high oxygen sticking coefficient to the bare Zr surface at the onset of the oxygen exposure (i.e. a low activation-energy barrier for oxide nucleation on the bare Zr surface) and/or a high activation-energy barrier for their further growth. (Indeed an oxygen sticking coefficient of unity has been reported for the bare Zr(0001) surface [50,51]). The oxide clusters thus are interpreted as oxide nuclei that have formed on the bare Zr surfaces at the onset of the oxidation process. The oxide nucleation on the terraces appears more homogeneous (random) on the bare Zr(0001) surface than on the bare 1×4-reconstructed Zr(10 $\bar{1}$0) surface (compare Fig. 3a and f).

As evidenced by the recorded STM images after 0.75 L O_2-exposure (see Fig. 3a and f), the consecutive processes of oxide nucleation, growth and coalescence to form a laterally-closed oxide layer are completed within 300 s of O_2-exposure at $T=450$ K and $pO_2=1\times10^{-4}$ Pa.[2]

Upon continued oxidation (i.e. $t>600$ s), the oxide clusters gradually restructure/reorient into bigger agglomerates: see Fig. 3a–e and f–j. The evolving oxide agglomerates have a characteristic lateral size of about 8 nm on the basal plane for $t=600$ s at $T=450$ K (see Fig. 3b), which by far exceeds the corresponding oxide-film thickness of 1.9 nm (as determined by RISE: see Table 1). For example, only three agglomerates are visible in the scanned STM area of 50 nm×50 nm, as recorded from the oxidized basal plane after 2400 s of oxidation (see Fig. 3d). The agglomeration process represents a gradual coarsening of the oxide structure, accompanied with an increase of the oxide-film roughness (cf. an increase of the root-mean-squared roughness values and the ΔZ values with increasing t; see caption of Fig. 3).

The upper valence band (UVB) region of the grown oxide films, as resolved from the measured XPS spectra of the Zr(10$\bar{1}$0) surface (for details, see Refs. [48]) after oxidation for successive oxidation times (i.e. 300, 600, 1800 and 7200 s) at $T=450$ K and $pO_2=1\times10^{-4}$ Pa, is shown in Fig. 4. The UVB region of zirconia is predominantly constituted of O2p states with some admixing by Zr (4 d and 5 s) states [53,54]. Evidently (see Fig. 4), the UVB region of the oxidized Zr(10 $\bar{1}$0) surface exhibits pronounced differences in shape with increasing oxidation time at $T=450$ K: i.e. for $t=300$ s the oxide-film UVB is rather flat and featureless, whereas for $t=7200$ s two distinct peak maxima at BE≈6.2 eV and BE≈8.5 eV have emerged. The higher BE side of the UVB, around the developing peak maximum of 8.5 eV, has a more bonding character, whereas the lower BE side of the UVB, around the evolving peak maximum of 6.2 eV, has a more non-bonding character [54]. As discussed in e.g. Refs. [42,43,48,55–57], a rather broad, featureless structure of the UVB is characteristic for a disordered (amorphous) phase with a relatively broad distribution of chemical bonding configurations. Indeed at $T<400$ K for $t=7200$ s [48], as well as for short oxidation times at $T=450$ K (see Fig. 4), the oxide films are still predominantly amorphous (as demonstrated by LEED, RHEED and XPS VB studies [48]). The gradual development of long-range order (and thus of specific bond configurations) in the oxide overgrowth, with increasing oxidation time at 450 K, results in the appearance of distinct bonding and non-bonding features in the UVB region: see Fig. 4. Hence a polycrystalline oxide film develops upon prolonged oxidation at 450 K, in accordance with HR-TEM [49] and RHEED [48] analyses.

As follows from the above discussion, the agglomeration of the oxide clusters (coarsening) with increasing oxidation time at $T=450$ K, as driven by the Gibbs–Thomson effect (see Section 2.1), is associated with the development of long-range order in the oxide overgrowths. Evidently, the coarsening of the oxide-film microstructure is thermally

[2] This observation is compatible with the preceding drop (at $L_{tot}=1.5$ and 2.5 nm for the Zr(0001) and Zr(10$\bar{1}$0) surfaces, respectively) of the oxide-film growth rate (cf. similar results in Refs. [6,52]), as measured by RISE [29,45].

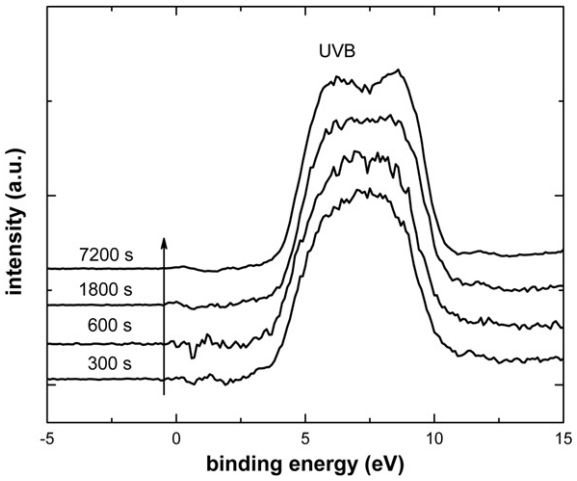

Fig. 4. Upper valence band (UVB) spectrum of the oxide overgrowths, as resolved from the measured XPS spectra of the Zr(10$\bar{1}$0) surface, after oxidation at $T=450$ K and $pO_2=1\times10^{-4}$ Pa for oxidation times of $t=300$ s, $t=600$ s, $t=1800$ s and $t=3600$ s. The arrow points in the direction of increasing oxidation time. For details on the spectral evaluation procedure, see Refs. [43,48].

activated at $T=450$ K (i.e. governed by kinetics). The initial oxide clusters, as formed on the bare metal surface after short oxidation times ($t\leq1200$ s) at $T=450$ K (i.e. before agglomeration), have an average lateral size in the range of 1.4–2.0 nm and are still (predominantly) amorphous (as concluded on the basis of the featureless shape of the resolved oxide-film UVB). Apparently, the development of long-range order in such a small oxide-cluster volume, characterized by a high surface-to-volume ratio, is obstructed (although short-range order can exist). A crystalline state only develops after longer oxidation times at $T=450$ K in parallel with the formation of bigger oxide agglomerates (compare Fig. 4 and Table 1).

As argued in Ref. [48], the strength of the Madelung field in the initially small oxide-cluster volumes could be too weak to realize the formation of a periodic arrangement of ions (i.e. the development of long-range order). Additionally, the amorphous state of the initial oxide clusters could also be favoured by the surface/interface thermodynamics (see Refs. [8,9,58]).

Although, the microstructure of the oxide overgrowth, as investigated by STM after $t=7200$ s at $T=450$ K (cf. Fig. 3i and j), does not reveal distinct facets, indicative of the formation of a well-defined crystalline oxide phase, the boundaries between the oxide agglomerates at e.g. $t=2400$ s can be conceived as the grain boundaries in the evolving polycrystalline oxide layer, as identified by cross-sectional HR-TEM in Ref. [49]; the densities of the boundaries between the oxide agglomerates (STM) and of the grain boundaries (HR-TEM) are comparable.

3. Conclusions

Exposure of the bare Zr surfaces to pure O_2(g) at substrate temperatures in the range of 300–450 K and at $pO_2=1\times10^{-4}$ Pa leads to the initial, very fast formation of a dense arrangement of small oxide clusters/protrusions; the whole surface is covered with oxide. The consecutive processes of oxide nucleation, growth and coalescence, leading to a "laterally-closed" oxide layer, have completed within $t=300$ s of O_2-exposure (at $T=300$–450 K and at $pO_2=1\times10^{-4}$ Pa). The average lateral size of the oxide clusters increases gradually with increasing oxidation time at constant oxidation temperature and with increasing oxidation temperature at constant oxidation time. The average lateral size of the oxide clusters after 7200 s of oxidation at $T=300$–450 K is in the range 1.2–4.2 nm (dependent on t and T).

The transport processes on the oxidizing surfaces become promoted with increasing temperature, thereby promoting the restructuring/reorientation of the oxide clusters into bigger agglomerates, e.g. with

increasing oxidation time at constant temperature, as driven by the Gibbs–Thomson effect.

At $T<400$ K for $t=7200$ s, as well as for shorter oxidation times at $T=450$ K, the oxide films are predominantly amorphous, because no long-range order can develop in the initially small oxide-cluster volumes. Long-range order in the oxide overgrowths only develops after longer oxidation times at $T=450$ K in parallel with the thermally-activated formation of bigger oxide agglomerates, which leads to the emergence of a characteristic fine structure in the resolved oxide-film upper valence-band spectrum as measured by XPS. The boundaries between the evolving oxide agglomerates are the grain boundaries in the evolving polycrystalline oxide layer.

References

[1] A.T. Fromhold, Theory of Metal Oxidation, North-Holland, City, 1976.
[2] E. Fromm, Kinetics of Metal-Gas Interactions at Low-Temperatures, Springer, City, 1998.
[3] D.A. King, D.P. Woodruff (Eds.), The Chemical Physics of Solid Surfaces and Heterogeneous Catalysis, Elsevier, Asterdam, 1990.
[4] A. Pasquarello, A.M. Stoneham, J. Phys. Condens. Mater. 17 (2005) V1.
[5] F.P. Fehlner, N.F. Mott, Oxid. Met. 2 (1970) 59.
[6] F. Reichel, L.P.H. Jeurgens, E.J. Mittemeijer, Acta Mater. 56 (2008) 2897.
[7] F. Reichel, L.P.H. Jeurgens, E.J. Mittemeijer, Surf. Interface Anal. 40 (2008) 281.
[8] F. Reichel, L.P.H. Jeurgens, G. Richter, P.A.v. Aken, E.J. Mittemeijer, Acta Mater. 55 (2007) 6027.
[9] F. Reichel, L.P.H. Jeurgens, G. Richter, E.J. Mittemeijer, J. Appl. Phys. 103 (2008) 093515.
[10] Y.M. Wang, Y.S. Li, K.A.R. Mitchell, Surf. Sci. 343 (1995) L1167.
[11] C.S. Zhang, B. Li, P.R. Norton, Surf. Sci. 313 (1994) 308.
[12] A. Stierle, V. Formoso, F. Comin, G. Schmitz, R. Franchy, Physica B 283 (2000) 208.
[13] R.A. Ploc, J. Nucl. Mater. 110 (1982) 59.
[14] R.A. Ploc, J. Nucl. Mater. 115 (1983) 110.
[15] E. Panda, L.P.H. Jeurgens, E.J. Mittemeijer, J. Appl. Phys. 106 (2009) 114913.
[16] H. Brune, J. Wintterlin, J. Trost, G. Ertl, J. Wiechers, R.J. Behm, J. Chem. Phys. 99 (1993) 2128.
[17] M. Muller, H. Oechsner, Surf. Sci. 387 (1997) 269.
[18] V. Maurice, S. Cadot, P. Marcus, Surf. Sci. 458 (2000) 195.
[19] F. Wiame, V. Maurice, P. Marcus, Surf. Sci. 601 (2007) 1193.
[20] F. Jensen, F. Besenbacher, E. Lægsgaard, I. Stensgaard, Surf. Sci. 259 (1991) L774.
[21] E. Panda, L.P.H. Jeurgens, E.J. Mittemeijer, Corros. Sci. 52 (2010) 2556.
[22] A. Wight, N.G. Condon, F.M. Leibsle, G. Worthy, A. Hodgson, Surf. Sci. 333 (1995) 133.
[23] F. Qin, N.P. Magtoto, M. Garza, J.A. Kelber, Thin Solid Films 444 (2003) 179.
[24] A.U. Goonewardene, J. Karunamuni, R.L. Kurtz, R.L. Stockbauer, Surf. Sci. 501 (2002) 102.
[25] G.F. Cotterill, H. Niehus, D.J. Oconnor, Surf. Rev. Lett. 3 (1996) 1355.
[26] W.X. Li, L. Österlund, E.K. Vestergaard, R.T. Vang, J. Matthiesen, T.M. Pedersen, E. Lægsgaard, B. Hammer, F. Besenbacher, Phys. Rev. Lett. 93 (2004) 146104.
[27] J. Klikovits, M. Schmid, L.R. Merte, P. Varga, R. Westerström, A. Resta, J.N. Andersen, J. Gustafson, A. Mikkelsen, E. Lundgren, F. Mittendorfer, G. Kresse, Phys. Rev. Lett. 101 (2008) 266104.
[28] K. Radican, S.I. Bozhko, S.R. Vadapoo, S. Ulucan, H.C. Wu, A. McCoy, I.V. Shvets, Surf. Sci. 604 (2010) 1548.
[29] G. Bakradze, L.P.H. Jeurgens, E.J. Mittemeijer, Surf. Interface Anal. 42 (2010) 588.
[30] A. Lyapin, L.P.H. Jeurgens, E.J. Mittemeijer, Acta Mater. 53 (2005) 2925.
[31] M.C. Gallagher, M.S. Fyfield, J.P. Cowin, S.A. Joyce, Surf. Sci. 339 (1995) L909.
[32] D.A. Bonnell, Prog. Surf. Sci. 57 (1998) 187.
[33] K. Meinel, K.M. Schindler, H. Neddermeyer, Surf. Sci. 515 (2002) 226.
[34] V. Maurice, M. Salmeron, G.A. Somorjai, Surf. Sci. 237 (1990) 116.
[35] J.M. West, Basic Corrosion and Oxidation, Elsevier, City, 1986.
[36] N. Stojilovic, E.T. Bender, R.D. Ramsier, Prog. Surf. Sci. 78 (2005) 101.
[37] C. Stampfl, M.V. Ganduglia-Pirovano, K. Reuter, M. Scheffler, Surf. Sci. 500 (2002) 368.
[38] M. Gutowski, J.E. Jaffe, C.L. Liu, M. Stoker, R.I. Hegde, R.S. Rai, P.J. Tobin, Appl. Phys. Lett. 80 (2002) 1897.
[39] G.D. Wilk, R.M. Wallace, J.M. Anthony, J. Appl. Phys. 89 (2001) 5243.
[40] D. Majumdar, D. Chatterjee, Thin Solid Films 206 (1991) 349.
[41] D. Majumdar, D. Chatterjee, Thin Solid Films 236 (1993) 164.
[42] J.M. Sanz, A.R. Gonzalezelipe, A. Fernandez, D. Leinen, L. Galan, A. Stampfl, A.M. Bradshaw, Surf. Sci. 309 (1994) 848.
[43] P.C. Snijders, L.P.H. Jeurgens, W.G. Sloof, Surf. Sci. 496 (2002) 97.
[44] A. Zalar, Thin Solid Films 124 (1985) 223.
[45] G. Bakradze, L.P.H. Jeurgens, E.J. Mittemeijer, J. Appl. Phys. 110 (2011) 024904.
[46] I. Horcas, R. Fernandez, J.M. Gomez-Rodriguez, J. Colchero, J. Gomez-Herrero, A.M. Baro, Rev. Sci. Instrum. 78 (2007).
[47] F. Wiame, V. Maurice, P. Marcus, Surf. Sci. 601 (2007) 4402.
[48] G. Bakradze, L.P.H. Jeurgens, E.J. Mittemeijer, J. Phys. Chem. C 115 (2011) 19841.
[49] G. Bakradze, L.P.H. Jeurgens, U. Starke, T. Acartürk, E.J. Mittemeijer, Acta Mater. 59 (2011) 7498.
[50] C.S. Zhang, B.J. Flinn, P.R. Norton, Surf. Sci. 264 (1992) 1.
[51] E. Fromm, O. Mayer, Surf. Sci. 74 (1978) 259.
[52] A. Lyapin, L.P.H. Jeurgens, P.C.J. Graat, E.J. Mittemeijer, Surf. Interface Anal. 36 (2004) 989.
[53] F. Zandiehnadem, R.A. Murray, W.Y. Ching, Physica B & C 150 (1988) 19.
[54] M. Morinaga, H. Adachi, M. Tsukada, J. Phys. Chem. Solids 44 (1983) 301.
[55] R.P. Gupta, Phys. Rev. B 32 (1985) 8278.
[56] M. Gautier, J.P. Duraud, L.P. Van, M.J. Guittet, Surf. Sci. 250 (1991) 71.
[57] M.H. Brodsky, M. Cardona, J. Non-Cryst. Solids 31 (1978) 81.
[58] L.P.H. Jeurgens, Z.M. Wang, E.J. Mittemeijer, Int. J. Mater. Res. 100 (2009) 1281.